Available online at www.sciencedirect.com

jmr&t Journal of Materials Research and Technology

journal homepage: www.elsevier.com/locate/jmrt

Ferritic layers formation mechanism during oxidation of FeMnSiCrNi alloys: Effect of temperature and influence on oxidation behavior

João Gabriel da Cruz Passos [a,b,**], Bruno Xavier de Freitas [c], Rodrigo da Silva [d], Carlos Alberto Della Rovere [d,*], Rodrigo Magnabosco [e], Marcelo Falcão de Oliveira [a], Artur Mariano de Sousa Malafaia [b]

[a] Engineering School of São Carlos, University of São Paulo, Av. João Dagnone, 1100 Jd Sta Angelina, São Carlos, SP 13563-120, Brazil

[b] Federal University of São João Del-Rei, Praça Frei Orlando, 170 Centro, São João Del Rei, MG 36307-334, Brazil

[c] Federal University of Itajubá, Avenida BPS, 1303, Pinheirinho, Itajubá, MG 37500-903, Brazil

[d] Munir Rachid Corrosion Laboratory, Federal University of São Carlos, Rodovia Washington Luis Km 235, São Carlos, SP 13565-905, Brazil

[e] Ignatian Educational Foundation, Av. Humberto A. C. Branco, 3972, Office K5-09, São Bernardo Do Campo, SP 09850-901, Brazil

ARTICLE INFO

Article history:
Received 30 May 2023
Accepted 3 October 2023
Available online 4 October 2023

Keywords:
High-temperature oxidation
FeMnSiCrNi alloys
Manganese-depleted layer
Phase transformation

ABSTRACT

Ferritic layer formation occurs after oxidation in Mn-rich austenitic alloys. It has significant effects on high-temperature oxidation resistance, but a better understanding of its formation is needed to control these effects. Thus, two FeMnSiCrNi alloys were exposed to six temperatures between 675 and 800 °C for 100 h. A relationship between mass variation and ferrite thickness was revealed, as Mn and Cr depletion occurred due to the $Mn_2O_3/MnCr_2O_4$ formation. Thermodynamic calculated phase diagrams indicated ferrite stability at high temperatures, affecting oxidation resistance. Finally, the Mn concentration profile changes during oxidation were studied with DICTRA analyses to explain the ferritic layer growth. By describing the growth and characteristics of this layer, the study can serve as a starting point for future investigations into designing more oxidation-resistant FeMnSiCrNi alloys.

1. Introduction

Austenitic FeMnSiCrNi alloys are shape-memory alloys (SMAs) developed as cheaper alternatives to traditional NiTi SMAs [1,2]. Despite their low manufacturing cost, good workability and weldability, studies in high temperatures have shown that they are prone to form non-protective oxide layers [3–5]. These results have motivated further investigations into their oxidation resistance and possible ways to increase it. Changing manganese (Mn), silicon (Si), and chromium (Cr) contents had some positive effects, as Mn tends to decrease oxidation resistance,

* Corresponding author.
** Corresponding author. Engineering School of São Carlos, University of São Paulo, Av. João Dagnone, 1100 Jd Sta Angelina, São Carlos, SP 13563-120, Brazil.
E-mail addresses: jgpassos@usp.br (J.G. da Cruz Passos), rovere@ufscar.br (C.A. Della Rovere).
https://doi.org/10.1016/j.jmrt.2023.10.026

while Si and Cr tend to increase it in FeMnSiCrNi as well as in Fe-based alloys in general [2,4–8]. However, some authors have indicated that there are limits to this strategy, with significant composition changes causing undesirable results such as increased mass gain rate, increased spallation and internal oxidation [4,9]. Furthermore, although Mn decreases oxidation resistance, its presence is essential, as it is an austenite stabilizer and plays a key role in enabling the shape-memory effect (SME) of these alloys [4].

Thus, the possibility of increasing oxidation resistance via compositional changes is limited. Consequently, different strategies have arisen, with promising results. Adding cobalt (Co), for example, has increased the oxidation resistance of an FeMnSiCrNi–Co alloy oxidized at 800 °C for up to 120h; however, the addition also increased the cost and promoted intermetallic phase formation [10]. Another strategy consisted of exposing FeMnSiCrNi alloys to a high-temperature vacuum atmosphere. In this atmosphere, Mn volatilized, forming a Mn-depleted layer on the treated samples [11]. These samples were then oxidized at 800 °C up to 24 h, and the authors verified an increase in oxidation resistance. In cyclic oxidation conditions, Mn depletion also increased the oxidation resistance of some FeMnSiCrNi alloys [12,13]. Initially, the alloys followed the expected behavior in cyclic oxidation tests (i.e., an increase in mass followed by spallation-induced mass loss); however, after a certain number of cycles, they started gaining mass again, prolonging their oxidation life. This renewed mass gain was caused by combined mechanical and chemical effects, both related to the reduced Mn availability in the metallic substrate and an austenite-to-ferrite transformation in the Mn-depleted layer.

Since Mn is an austenite stabilizer, its depletion causes the destabilization of the austenitic structure and the formation of a Mn-depleted ferritic layer [11,12,14,15]. This layer, as discussed, can be used to increase the oxidation resistance of FeMnSiCrNi alloys [11]. However, it can also be detrimental, as a previous study has shown by oxidizing two FeMnSiCrNi alloys at 800 °C [6]. The alloy with a higher amount of ferritizing elements and a lower amount of austenite stabilizers had a lower oxidation resistance. The behavior was attributed to faster ferrite formation in this alloy during exposition to elevated temperatures. Another study has shown that Mn diffuses faster in ferrite than in austenite, which is responsible for an oxidation rate increase when this structure is stable at the oxidation temperature. Ferrite stabilization during oxidation can occur due to a sufficiently severe Mn depletion. If the depletion is insufficient, the ferritic layer forms only upon cooling. Ferrite forms more readily and at lower temperatures in FeMnSiCrNi alloys with higher contents of ferrite stabilizers and lower contents of austenite stabilizers [3,14]. At room temperature, the ferritic layer usually has an almost constant Mn concentration through its thickness whether it was present at the oxidation temperature or not. Upon crossing the ferrite-to-austenite boundary, Mn content rises rapidly to values close to or equal to the initial concentration [14]. Finally, Cr also takes part in the oxidation process of these alloys and, as a ferritizing element, its depletion could affect ferrite formation [6].

Ferritic layers formed due to Mn depletion are observed in several studies with austenitic FeMnSiCrNi alloys. However, the diffusion behavior of Cr and Mn that causes and is caused by the formation of this layer could be better understood. The concentration gradient of these elements, especially, was discussed only as they were observed at room temperature. The ferrite layer is very important to the oxidation behavior of FeMnSiCrNi alloys and can potentially be used to increase their oxidation resistance. Thus, the present study investigated the isothermal oxidation of two FeMnSiCrNi alloys between 675 and 800 °C for 100 h, focusing on the relationship between the ferritic layer, temperature, and mass variation. The oxidized samples were characterized with SEM/EDS (Scanning Electron Microscope equipped for Energy-Dispersive X-ray spectroscopy) and XRD (X-Ray Diffraction). Furthermore, thermodynamic calculated phase diagrams, Thermo-Calc's Diffusion Module (DICTRA) and empirical data were used to understand the formation mechanism of the ferritic layer and its impact on the oxidation behavior.

2. Experimental

The oxidation behavior of two FeMnSiCrNi alloys was investigated. Their composition is shown in Table 1, measured using inductively coupled plasma optical emission spectroscopy (ICP-OES). Compared to Alloy B, Alloy A has a lower quantity of ferritizing elements and protective oxide formers (Cr and Si). Alloy A also has a lower Ni content, which is an austenitizing element. It has a higher Mn content, another austenitizing element. As a previous study has shown, slight variations in composition can cause large differences in oxidation behavior for these alloys. Furthermore, these slight variations can affect the alloy properties without sacrificing the shape-memory effect [6].

The alloys were cast in a vacuum induction furnace, using as base raw material an AISI 304 stainless steel in bulk form, to which high-purity raw materials were added. After casting, alloys were hot-rolled at 1000 °C and solubilized at 1050 °C for 1 h followed by water quenching. For oxidation tests, rectangular samples were cut with a surface area of approximately 5 cm^2. These surfaces were prepared with up to #600 grit SiC sandpaper. The surface preparation process is done to standardize the surface roughness of the samples. Before oxidation, the samples were degreased and cleaned with an ultrasound bath using isopropyl alcohol as a cleaning fluid.

The samples were measured, weighed, and then oxidized for 100 h at six different temperatures: 675, 700, 725, 750, 775, and 800 °C. At each temperature, two samples of each alloy were tested. After the end of the test, they were furnace-cooled and weighed again. The average mass variation per area of the samples was computed and statistical differences between the values in each condition were evaluated with ANOVA. To characterize the oxide layer, the samples were

Table 1 – Chemical composition of alloys A and B in mass % as measured by ICP-OES.

Alloy	Mn	Cr	Si	Ni	Fe
A	13.67	8.32	3.46	3.04	Balance
B	13.04	9.56	3.77	3.55	Balance

evaluated with X-ray diffraction (XRD) analysis (Cu-Kα radiation, scanning from 20 to 90° in θ/2θ geometry). After these processes, the samples were cross-sectioned and embedded in Bakelite. They were then ground and polished by sanding with up to #1200 grit SiC sandpaper and then polished in a 1 μm alumina abrasive emulsion, exposing the cut cross-section.

For FeMnSiCrNi alloys, "ferritic layer" and "Mn-depleted layer" are often used interchangeably. This was done due to the several previous studies which have shown that the severe degree of Mn depletion usually observed close to the surface of FeMnSiCrNi alloys causes austenite destabilization. Because Mn diffuses faster in ferrite, this leads to a severe depletion of the element in this region, making the boundary between ferrite and austenite easily identifiable [6,9,14]. As the results will show, this was the case for all test conditions in this study, and the ThermoCalc also indicated austenite destabilization. For this reason, in this study the Mn-depleted layer was also referred to as a ferritic layer.

The thickness of the ferritic layer formed during oxidation was measured with optical microscope images. The ferritic layer has different mechanical properties than the austenitic substrate [16]; consequently, it responds differently to grinding and polishing. Thus, in an optical microscope, the area occupied by the ferritic layer could be detected and by its darker color with ImageJ, a public-domain image analysis software, and then measured. By dividing this area by the image length, the average layer thickness was determined. A total length of 0.5 mm was analyzed in each sample in this measurement. The chemical composition of the oxide layers and metallic substrate adjacent to the oxide layers was determined in a scanning electron microscope (SEM) equipped for energy-dispersive X-ray spectroscopy (EDS). The Mn and Cr contents in the ferritic layer were computed and changes in these concentrations as a function of the distance from the oxide were evaluated with line scans. To avoid comparisons between values obtained from different measurement methods, these results were not compared with the composition determined by ICP-OES (Table 1), but with the composition determined by EDS analysis of non-oxidized samples.

The ferritic layer formation was also studied. A possible relationship between ferritic layer thickness and mass gain was theorized, and results from previously published studies were compared to this theory. To better comprehend the ferritic layer stability during the oxidation process, various Mn–FeSiCrNi pseudo-binary phase diagrams were calculated with ThermoCalc software. Considering the possible Cr depletion effects, diagrams were constructed with the alloys at the composition shown in Table 1 and at 6 wt % Cr. Table 2 shows the initial composition for each diagram.

Diffusion simulation analysis was performed using the DICTRA module of ThermoCalc to investigate changes in the Mn chemical gradient at the ferrite/austenite interface (for alloy A composition) during isothermal exposure and cooling. These tests involved simulating the diffusion behavior of Mn between a Mn-rich (fcc) and a Mn-depleted (bcc) region. The large difference in Mn concentration between these two regions facilitates the diffusion of Mn from austenite to ferrite, as is the case during oxidation. With the simulations, it was possible to study changes in the position and Mn distribution at the austenite/ferrite interface during high-temperature exposure. First, the behavior during isothermal exposure (1 h at 800 °C) was analyzed by assuming an initially "perfect" interface, with a Mn-depleted (1.5 wt%) ferrite and an austenitic substrate with the initial composition of the alloy. Additionally, a situation with a ferritic layer without Mn (0 wt%) was also studied, since the simulations do not account for Mn lost by oxidation and, therefore, Mn diffusion to ferrite is probably underestimated in the first case. Finally, an analysis of the cooling process was done, whereby the system was cooled from 800 °C to 400 °C in 5 min.

Table 2 – Initial conditions used to calculate the phase diagrams for alloys A and B, in mass %. Note that as Cr is depleted, the relative Mn, Si, Ni and Fe amounts increase accordingly.

Condition	Alloy	Mn	Cr	Si	Ni	Fe
Initial composition	A	13.67	8.32	3.46	3.04	Balance
	B	13.04	9.56	3.77	3.55	Balance
Cr-depleted	A	14.02	6.00	3.55	3.12	Balance
	B	13.55	6.00	3.92	3.69	Balance

3. Results

3.1. Mass variation

The average mass variation for each alloy at each temperature is shown in Fig. 1. Alloy A gained, on average, more mass at all temperatures from 725 to 800 °C, while alloy B gained more mass at 700 °C. The p-values associated with each temperature are shown in Fig. 1. P-values lower than 0.1 (90 % confidence) were considered significant in this study, showing that the difference in oxidation resistance was statistically significant only at 700 °C.

3.2. Oxide composition

Fig. 2 shows the oxide layer of samples of alloys A and B oxidized at 700, 725 and 800 °C (results at the other temperatures were not significantly different and thus were omitted for brevity). Mainly Mn and Cr appeared in the oxide layers of both alloys. Mn oxides predominated in the external part of the oxide layer and a Mn–Cr-rich oxide appeared in the internal region, close to the substrate (as indicated by the significant Cr and Mn contents on the inner part of the oxide layer). As the EDS maps show, a Mn-depleted zone was formed below the oxide layer. This zone also had a lower Cr content than the substrate.

According to XRD analysis at 675, 725 and 775 °C, shown in Fig. 3, only Mn_2O_3 and a Mn–Cr spinel ($MnCr_2O_4$) were detected. Again, results at other temperatures were omitted for brevity, as no other oxides could be observed. The diffraction patterns from alloys A and B are similar, a reflection of the similarity in mass variation behavior. As in some previous studies, the peak at approximately 82.5° corresponds to the ferritic substrate. This is the only lone ferrite peak that can be observed, as the two remaining peaks coincide with oxide peaks [9,14,17]. Furthermore, the observation of this

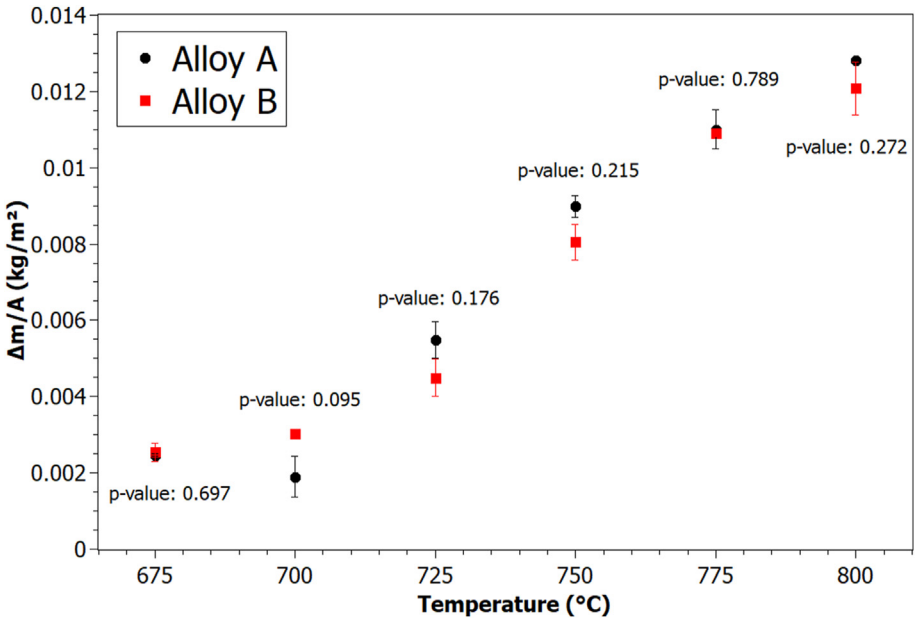

Fig. 1 – Mass variation per surface area as a function of temperature for each alloy after 100 h of oxidation. P-values correspond to ANOVA comparing alloys A and B at each temperature.

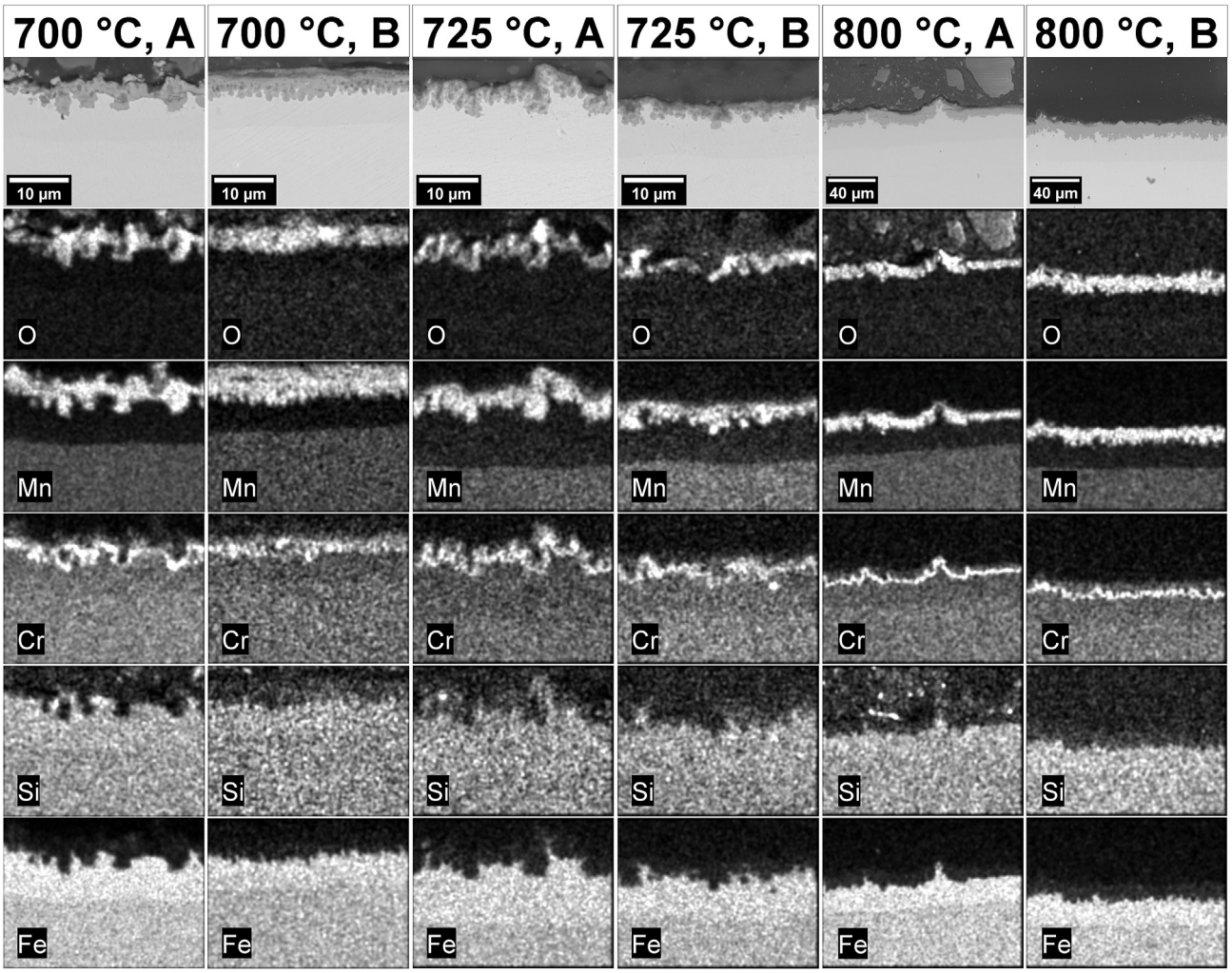

Fig. 2 – Cross-section EDS maps of Fe, Mn, Si, Cr and O of samples of alloys A and B oxidized at 700, 725 and 800 °C, for 100 h.

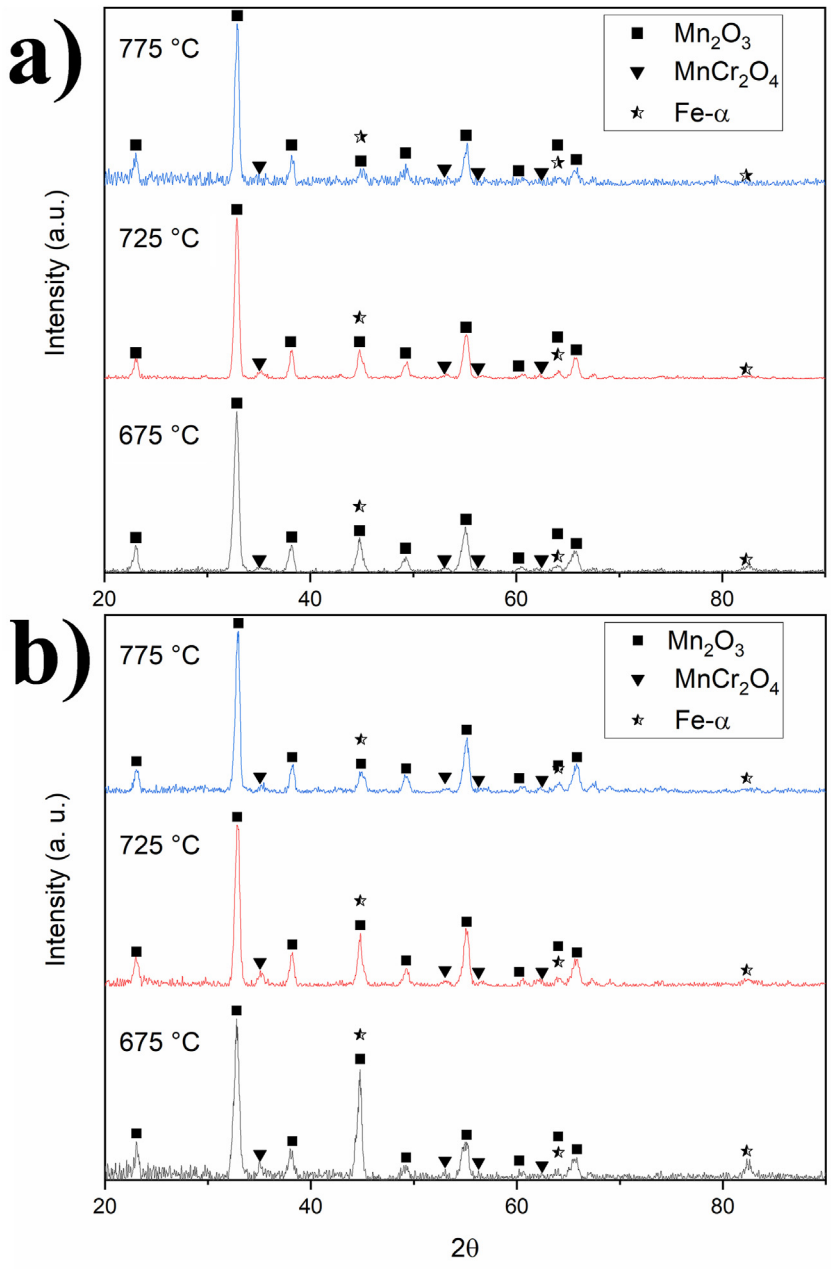

Fig. 3 – XRD analysis of samples of alloy A (a) and alloy B (b) oxidized at 675, 725 and 775 °C, for 100 h. Small unidentified peaks are related to Mn_2O_3 or $MnCr_2O_4$.

peak indicates that the oxide layer was thin enough to allow x-ray penetration through to the substrate.

3.3. *Mn-depleted layer thickness*

The Mn-depleted layer thickness of each sample was measured and plotted as a function of mass variation in Fig. 4. The line fits for alloy A, for alloy B, and both alloys are also presented. To study the relationship between mass variation and ferrite thickness among different FeMnSiCrNi alloys, results from numerous studies were consolidated in Fig. 5. Only data from isothermal oxidation tests or cyclic oxidation tests before spallation occurred were considered. The "all data" linear fit corresponds to all the data points shown in the figure, and the inset data corresponds to the data shown in the inset graph.

3.4. *Mn-depleted layer composition*

Mn and Cr contents of the ferritic layers and the austenitic substrates evaluated by EDS are shown in Fig. 6. The Mn content in the ferrite decreased between 675 and 700 °C, increased again at 750 °C and oscillated at a similar level at the other temperatures. Cr content also varied nonlinearly through the different temperatures, but it was higher in the ferritic layers formed at 675 and 700 °C. In general, the ferritic layer of alloy B was poorer in Mn and richer in Cr (at 675 and 700 °C, it was poorer in both Mn and Cr).

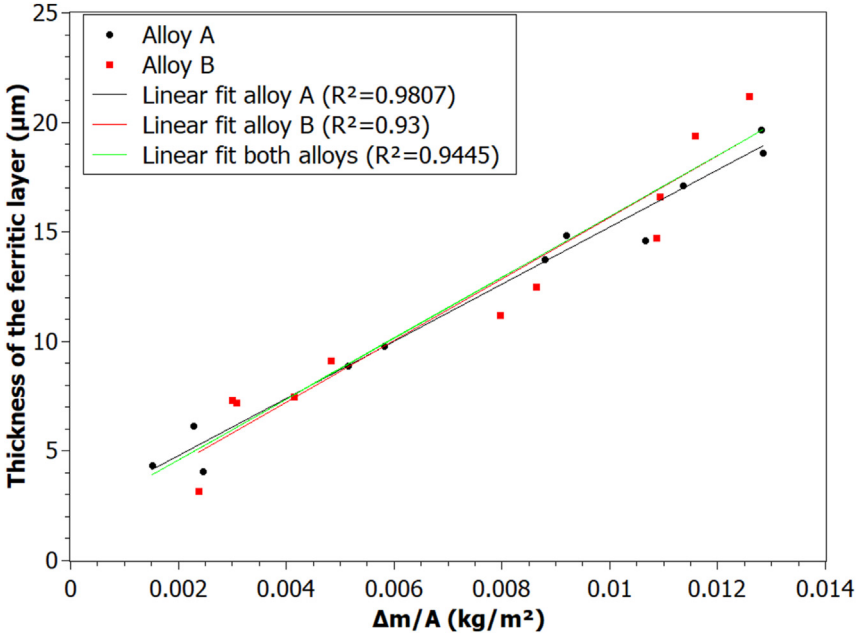

Fig. 4 – Line fit for the ferrite layer thickness as a function of mass variation for alloys A and B separately and for both alloys at once.

The Mn and Cr composition gradient through the ferritic layer was similar in all test conditions as illustrated by Fig. 7, which corresponds to the samples oxidized at 775 °C. Because of the similar gradients at every test temperature, only results at 775 °C are presented. There was a slight Mn concentration gradient in the ferritic layer, with Mn content increasing from the oxide layer to the austenitic substrate. At the ferrite/austenite interface, the variation in Mn content was sudden,

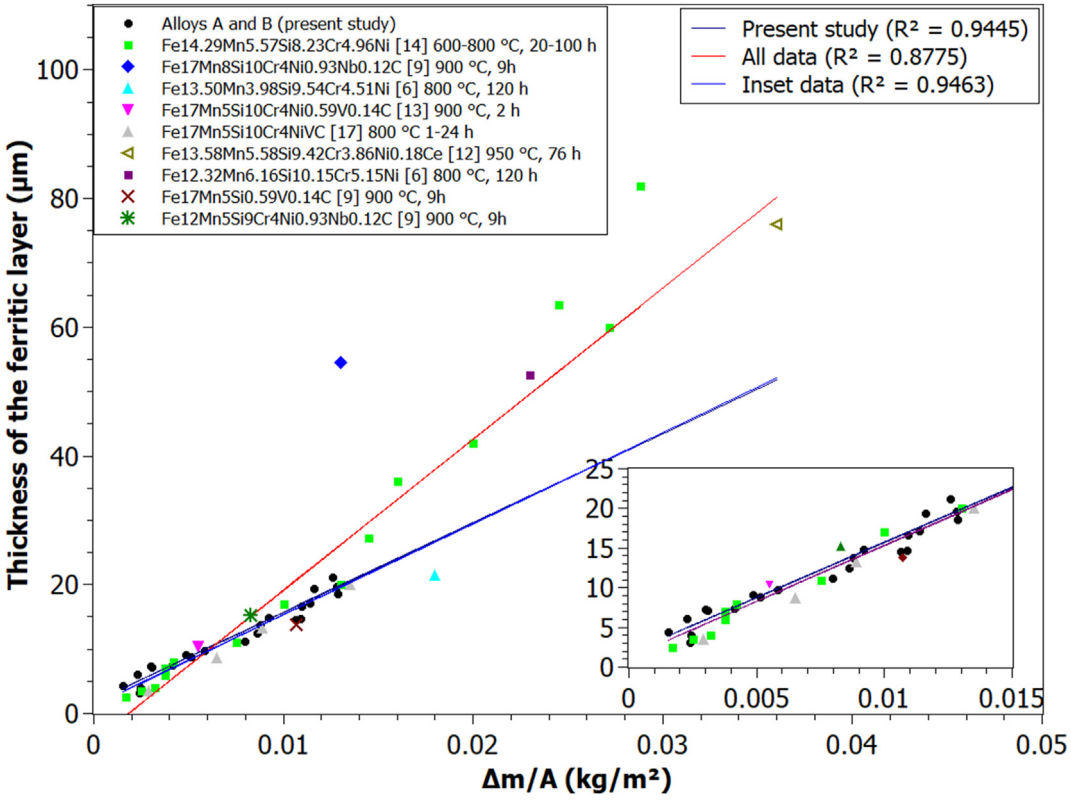

Fig. 5 – Ferrite thickness as a function of mass variation for various FeMnSiCrNi alloys. Inset shows data points fitted to the blue line.

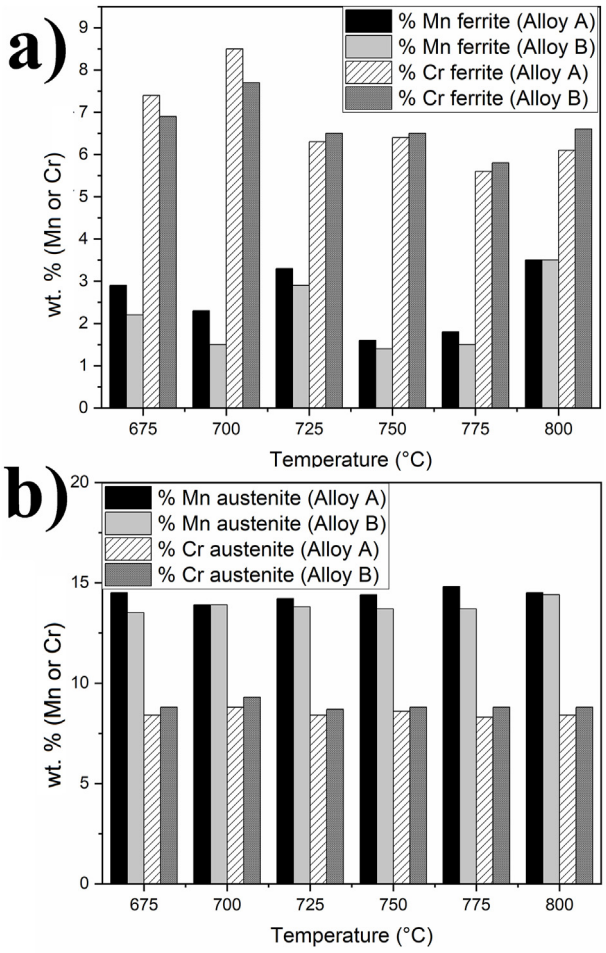

Fig. 6 – Mn or Cr content (mass %) in the ferritic layer (a) and the austenitic substrate close to the ferritic layer (b).

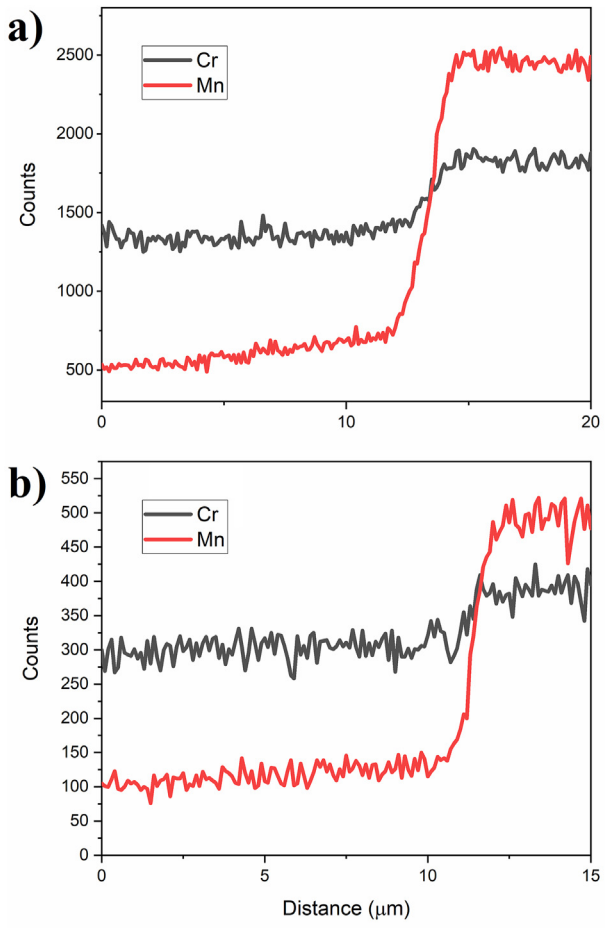

Fig. 7 – Mn and Cr concentration as a function of distance from the oxide layer in alloy A (a) and alloy B (b), both oxidized at 775 °C for 100 h.

rapidly reaching the original alloy composition. There was still a Mn gradient between the Mn content of ferrite and the Mn content of austenite (i.e., it did not change directly), but because the gradient was very steep, the interaction volume of the electron beam should be considered (the EDS signal at each position originates from a certain volume of the sample around the measurement position). When the beam approaches the ferrite/austenite interface, signals from both phases are collected, giving origin to an artificial concentration gradient in the resulting line scan that masks the real gradient. Cr was also depleted in the ferritic layer of both alloys, and the original Cr composition was reached only in the austenitic substrate.

3.5. *ThermoCalc and DICTRA analyses*

Fig. 8 shows a pseudo-binary Mn–FeSiCrNi phase diagram for alloy A at its initial composition determined by ICP-OES. This phase diagram depicts changes in microstructure as Mn content decreases. On the diagram, two points are marked at each of the six test temperatures. They correspond to the maximum amount of Mn that can be dissolved on ferrite before it becomes supersaturated, hereby called Mn_{fer}, and the minimum Mn content required to keep austenite stable, hereby called Mn_{aus}. Naturally, ferrite is stable with Mn contents lower than Mn_{fer}, and austenite is stable with contents above Mn_{aus}. For Mn contents between Mn_{fer} and Mn_{aus}, both phases (ferrite and austenite) are stable. In this case, what happens is the coexistence of two phases, and a local equilibrium at the interface respecting Mn_{fer} and Mn_{aus} at a specific temperature. Concerning ferrite stability, an increase in Mn_{aus} indicates that it becomes easier to form ferrite (less Mn needs to be lost). An increase in Mn_{fer} indicates that more Mn can be dissolved in ferrite. The twelve values were computed for alloys A and B at their initial composition, and also at a lower Cr content, accounting for Cr depletion during oxidation. The values are shown in Fig. 9.

The changes in the austenite/ferrite interface for up to 1 h of exposure at 800 °C as predicted by DICTRA are shown in Fig. 10. In Fig. 10a, which considers an initial ferrite composition of 1.5 wt% Mn, it is possible to see that the concentration gradient in austenite softened. This change, however, was small, occurring along a less than 1-μm thick layer. Despite becoming less steep, the Mn content always drops abruptly at the ferrite/austenite interface, as pointed out in 1. Mn content tended to increase slightly and stabilize at a value close to 1.6 wt%; consequently, there was almost no Mn gradient in the ferritic layer at the end. In Fig. 10b, the increase in Mn content

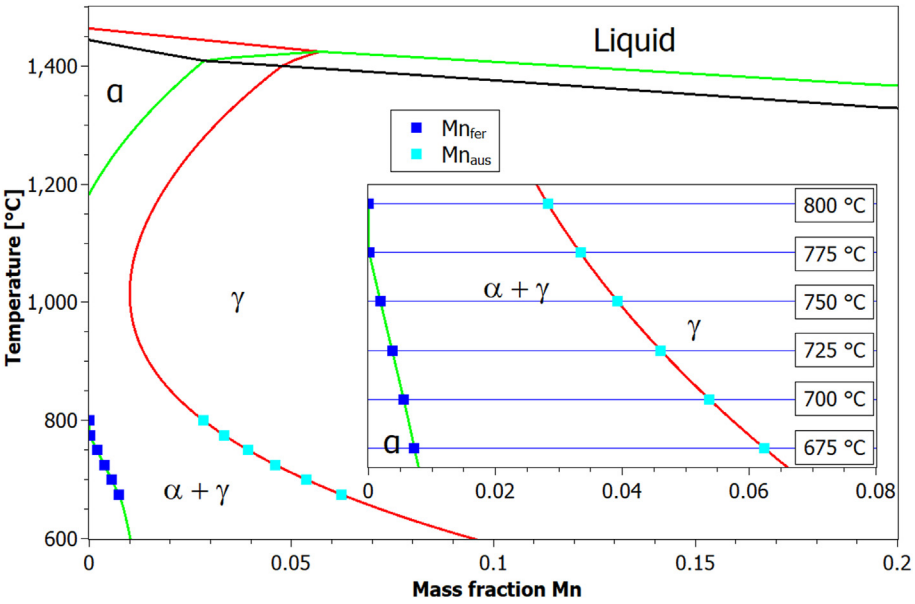

Fig. 8 – Calculated phase diagram for alloy A (initial composition). Inset details test temperatures, Mn_{fer} and Mn_{aus}.

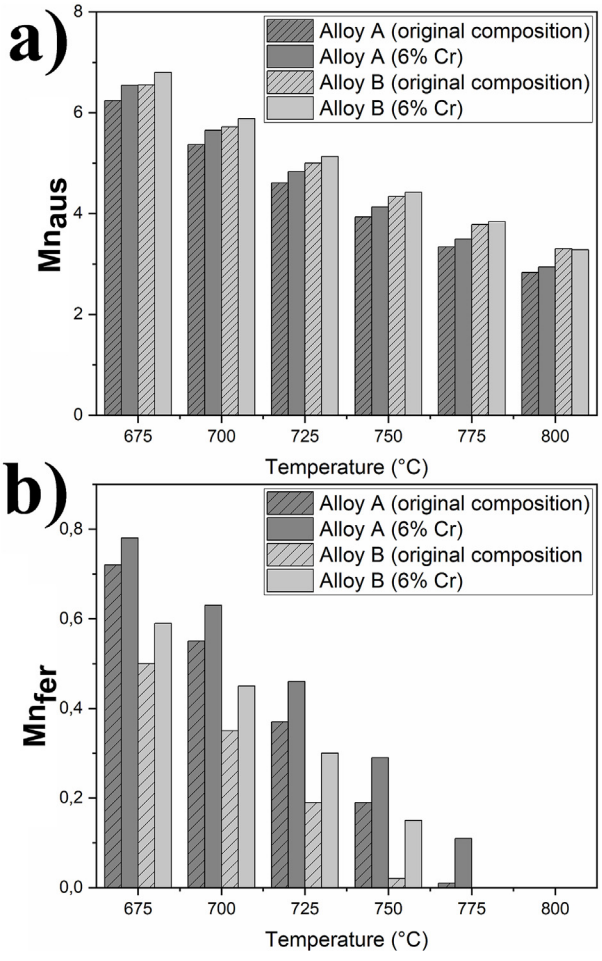

Fig. 9 – Changes in Mn_{aus} (a) and Mn_{fer} (b) with increasing temperature for alloys A and B, according to calculated phase diagrams.

was more severe, going from an initially Mn-free layer to one with approximately 0.98 wt% Mn. A Mn gradient could be seen in ferrite even at the end of the process. However, as in the previous case, the gradient (both inside ferrite and in the ferrite/austenite interface) softened with increasing exposure time.

Finally, the analysis of the cooling process is shown in Fig. 11. During cooling, Mn enrichment of the region of the ferritic layer that is closest to austenite occurred, as well as a depletion of Mn in austenite. Furthermore, as the inset shows, the increase in Mn_{aus} caused the direct drop in Mn concentration to become more pronounced as temperature decreased. This is accompanied by a slight growth of the ferritic layer. These are very small alterations, lengthwise, with the Mn enrichment in ferrite occurring along a length of approximately 0.5 μm and the ferrite layer growing less than 0.015 μm. Also, while the diffusion of Mn from austenite to ferrite causes the Mn gradient to become smoother, the increase in Mn_{aus} causes it to become steeper.

4. Discussion

4.1. *Oxidation resistance*

The difference in mass variation between alloys A and B was significant only at 725 °C (alloy A gains more mass). The mass variation was positive in all temperatures and increased with temperature (except between 675 and 700 °C). A behavior change seems to have occurred between 700 and 725 °C for alloy B and between 675 and 700 °C for alloy A. This can be observed with an ANOVA comparing the mass variation of each alloy at 700 °C with the variation at 725 °C. In this case, the p-value indicated the significance of the change in mass variation between the two temperatures for each alloy. The p-value for alloy A (0.019) was much smaller

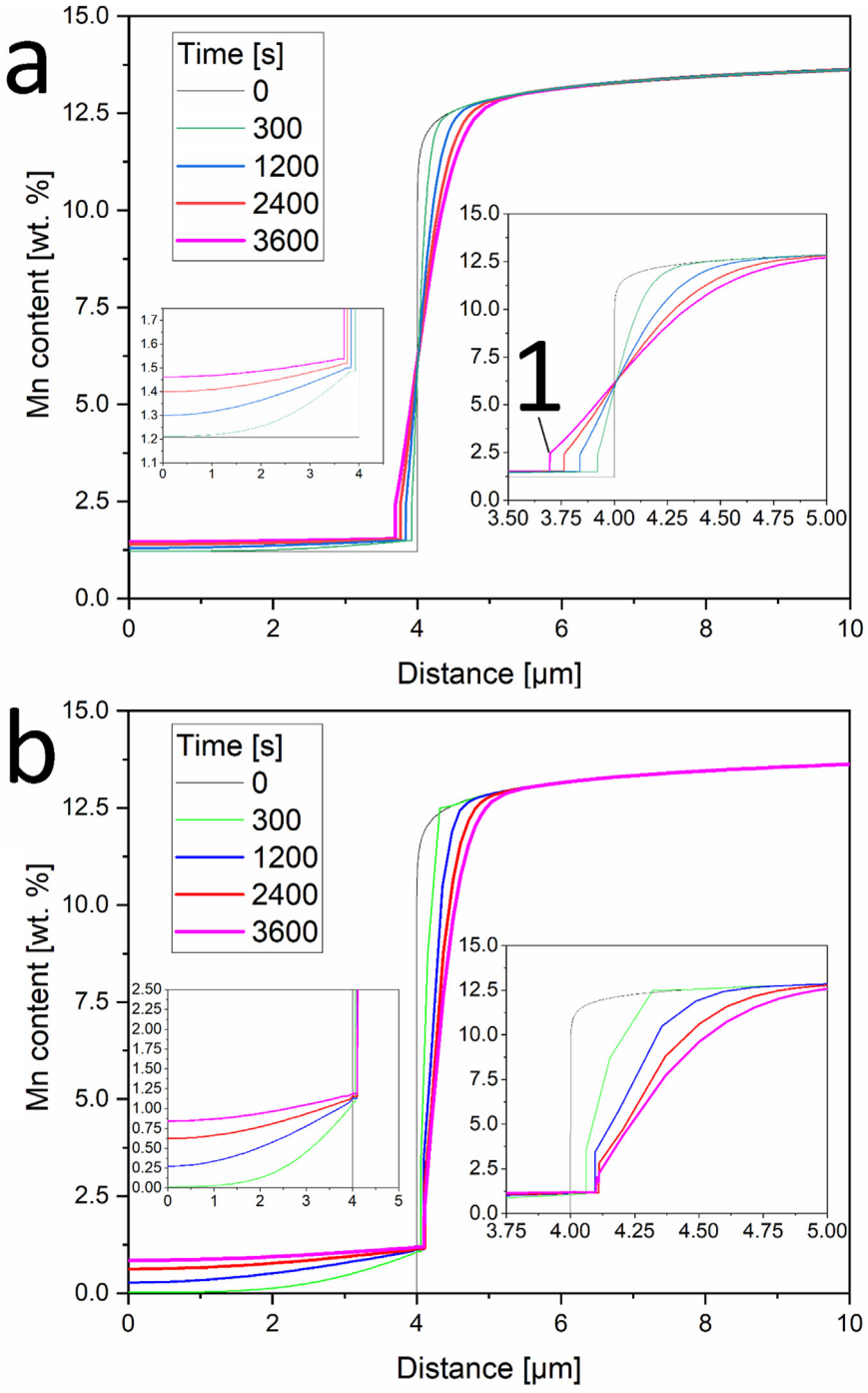

Fig. 10 – DICTRA simulations of Mn diffusion in a ferrite/austenite interface after 1 h of exposure at 800 °C with an initial Mn content in ferrite of 1.5 wt % (a) and 0% (b). The direct change in Mn composition at the ferrite/austenite interface is detailed in 1.

than for alloy B (0.053), indicating that the change in alloy B was of lower significance. This sudden change in oxidation behavior seems to be associated to some degree with ferrite stability. A higher tendency for ferrite formation was already associated with decreased oxidation resistance [6]. A similar phenomenon may have occurred here, with ferrite forming more readily in alloy B at 700 °C. With an increase in temperature to 725 °C, ferrite stability decreases. The same reasoning can be used to explain the higher average mass gain of alloy A at 675 °C than at 700 °C. Because the formation of ferrite in alloy A requires a more severe Mn depletion than in alloy B at any given temperature (Fig. 9), this behavior change occurred at a lower temperature (between 675 and 700 °C).

As previously mentioned, the difference in mass variation between the alloys themselves is only significant for a

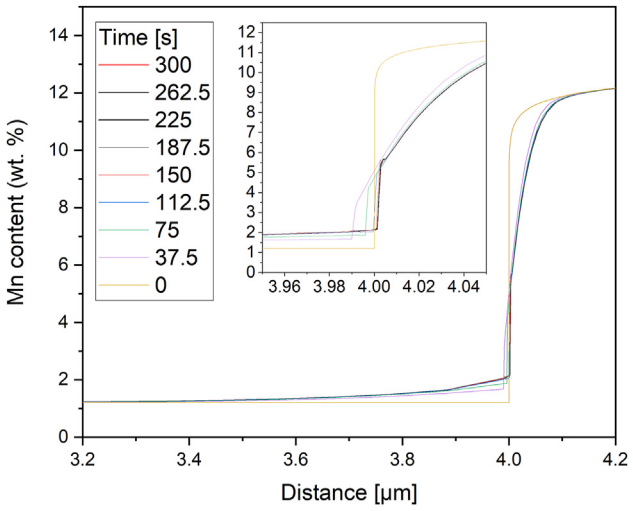

Fig. 11 – DICTRA simulations of Mn diffusion after cooling from 800 to 400 °C in 5 min.

confidence interval of 90 % at 700 °C. In all the other cases, although the average mass variation differs, the difference is not statistically significant. To gauge which of the two alloys has a higher oxidation resistance, a larger number of experiments would have to be run. However, the experimental design chosen here was successful in showing an alteration in the behavior of the alloys with increasing temperature (between 675 and 700 °C for A and between 700 and 725 °C for B), which was its primary objective.

The similarities in oxidation resistance of both alloys were also seen in their oxide layers, which are similar to other FeMnSiCrNi alloys. The presence of Mn_2O_3 and a Mn–Cr spinel ($MnCr_2O_4$) in the relative positions seen in Fig. 2 was previously observed in studies with these alloys [3,6,10,17]. Spinel crystalline peaks were more apparent in alloy B, indicating that Cr might have a larger role in the oxidation process of this alloy. With increasing temperature, there was a reduction in the intensity of spinel and α-iron crystalline peaks. This was a consequence of an increase in the oxide layer thickness, as more of the external Mn oxide layer was detected, instead of the internal spinel layer or the substrate. In conclusion, analysis of EDS and XRD results do not indicate a relationship between oxide composition and the poorer mass variation behavior in lower temperatures. Finally, Si oxide, seen in some of these studies, was not identified here. This was possibly a consequence of the Si oxide layer formed in FeMnSiCrNi alloys being usually thin and discontinuous [3]. However, the oxide layer of samples oxidized at 675 °C exhibited a higher average Si content (3 wt %) than at 800 °C (1 wt %), according to an area EDS analysis of both oxide layers, which shows that silica formation cannot be discarded.

At 700 °C and at 675 °C (not pictured), the Mn–Cr rich spinel is less apparent than at 725 and at 800 °C, even though it can still be observed. This agrees with the Mn–Cr–O phase diagram [18], which shows that lower temperatures favor the formation of Mn oxides over Mn–Cr spinel. It is possible that, at lower temperatures, this lower tendency for spinel formation, combined with the high Mn diffusion rates in ferrite, hinders the formation of a continuous spinel layer. Although this is true for both alloys A and B, the Cr signal in the oxide layer of alloy B appears to be more diffuse than in alloy A, which indicates a less continuous and compact Cr–Mn spinel oxide layer. The easier ferrite formation in alloy B could delay the formation of such spinel layer even further, which would explain its behaviour, as well as the reduced oxidation resistance of the alloy at this temperature. As the temperature increases, both alloys can form a more protective spinel layer and the protective effect of the higher Cr and Si contents in alloy B predominates.

4.2. *Relationship between ferritic layer thickness and mass variation*

Regarding the proposed relationship between ferritic layer thickness and mass variation, the quality of the fit in Fig. 4 was good for alloys A and B when analyzed separately (R^2 of 0.9807 for A and 0.9300 for B). When data from both alloys were included at once, the linear fit was still good (R^2 of 0.9445, better than for the alloy B samples alone), indicating that the relationship between ferrite thickness and mass variation was similar for both alloys. Such a relationship was already observed in a previous study with FeMnSiCrNi alloys [16]. The R^2 value calculated from the aggregate of various FeMnSiCrNi alloys (Fig. 5) was lower than the one observed for the alloys in this study (R^2 of 0.8775), indicating that the thickness to mass variation ratio was different in some cases. Alloy Fe17Mn8Si10Cr4Ni0.93Nb0.12C [9] oxidized at 900 °C for 9 h, for example, formed a much thicker ferritic layer, which might be related to the ferritizing potential of Si. This alloy was also submitted to 9 1-h cycles, instead of continuous exposure to high temperatures. However, other alloys that were exposed to cyclic tests, such as Fe17Mn5Si10Cr4Ni0.93Nb0.12C [9], Fe17Mn5Si10Cr4Ni0.93Nb0.12C [9], and Fe17Mn5Si10Cr4NiVC [13], presented a thickness to mass gain ratio similar to the alloys studied here.

The deviation from the proposed linear behavior seems to be specific to thicker ferrite layers. In samples with a mass variation below 0.015 kg/m^2, the ferrite layer formed in alloy Fe14.29Mn5.57Si8.23Cr4.96Ni [14] followed a thickness-to-mass variation ratio close to that of Alloys A and B. However, as the ferrite layer thickness increased, so did the deviation from the expected behavior for the referenced alloy. A linear model that does not take thicker ferrite layers into account is shown in Fig. 5 inset, with an R^2 of 0.9463. The fit, almost equal to the one observed for the alloys in this study, was evidence of a common relationship between the two variables among different alloys and test conditions in this mass variation/ferrite layer thickness range.

4.3. *Formation and composition of the Mn-depleted layer*

The Mn-depleted layers of all alloys in all test conditions shared common characteristics, such as the relationship between thickness and mass variation and the overall features of the ferrite/austenite interface. Ferrite (bcc) was also stable at the oxidation temperatures in both alloys between 675 and 800 °C. They initially had an austenitic fcc structure, as indicated by ThermoCalc. The observation of a more severe Cr

depletion at higher temperatures in both alloys indicates that Cr participation in the oxidation process increased with temperature. This agrees with Mn–Cr–O phase diagrams, which predict an increase in the fraction of Mn–Cr spinel as temperature increases [18].

As for ferrite formation and its effect on oxidation, ThermoCalc predicted that Mn_{fer} and Mn_{aus} decrease with temperature. Thus, the formation of ferrite was easier, and the phase could dissolve more Mn as temperature decreased. The easier formation and increased availability of Mn in ferrite at lower temperatures could be responsible for the increased mass variation at 675 and 700 °C. Cr depletion also affected ferrite stability, as lower Cr content increases Mn_{fer} and Mn_{aus}. Thus, with Cr depletion, ferrite forms more readily and can accommodate a larger Mn content. The noticeably higher Cr depletion in the ferritic layer was caused by the element's higher diffusion rate in ferrite than in austenite [19]. This could result in another positive effect of the presence of a ferritic layer during oxidation. As previously discussed, the presence of ferrite can have a positive effect, as the low Mn content reduces the oxygen pressure of the element [11]. A negative effect of ferrite stability at the oxidation temperature which was already pointed out is that Mn diffusion is faster in ferrite [14]. This logic, however, could also be applied to Cr to describe yet another positive effect of the ferritic layer, as the diffusion rate of the element also increases.

Concerning the differences in oxidation behavior between both alloys, according to ThermoCalc, the depletion of Mn causes the formation of ferrite earlier in alloy B than in alloy A (alloy B has a higher Mn_{aus}). The easier ferrite formation in alloy B could increase its oxidation rate. However, except at 800 °C, Mn_{fer} is higher in alloy A than in alloy B (this is confirmed by the EDS measurements in Fig. 6). The higher amount of Mn dissolved in alloy A could increase Mn availability, also increasing the oxidation rate. Thus, there are features to the ferritic layer formation that could comparatively increase the oxidation resistance of both alloys, which would explain their similar oxidation behavior. To better understand the magnitude of those effects, new studies with more alloys of different compositions should be undertaken.

According to DICTRA simulations of isothermal exposure, the tendency seems to be to diffuse Mn from austenite to ferrite, even if ferrite is supersaturated, moving the ferrite/austenite interface in the direction of the ferritic layer. However, the model does not consider the loss of Mn to oxidation. Thus, this movement of the interface to the ferritic layer was limited by the consumption of the element, with little change in ferrite composition. The tendency for ferrite to exist in a supersaturated state and for the ferrite layer to grow when a significant amount of Mn leaves austenite can be seen in the analysis with a completely Mn-depleted ferritic layer. In this case, because a larger amount of Mn diffused to ferrite, the interface moved in the direction of the austenitic substrate, and ferrite reached a Mn content of about 0.98 wt%, above its solubility limit of Mn in this phase at 800 °C (which is 0). Also, the direct change in Mn composition (Fig. 10) is related to the saturation of the element. ThermoCalc predicted a Mn_{aus} of around 2 % for alloy A, which is close to the Mn content in which the drop occurs. Thus, this drop in composition occurs between the true Mn_{fer} and Mn_{aus} values, as DICTRA assumes a local equilibrium at the ferrite/austenite interface.

During cooling, the Mn concentration gradient suffers some minor changes, which seem to be dictated by the increase in Mn_{aus} as temperature decreases (3 wt% at 800 °C to 6.3 wt% at 800 °C). This destabilizes the austenite region close to the ferrite/austenite interface, which has a reduced Mn content. As a result, Mn diffuses to ferrite, increasing the Mn content of this phase. The increase in Mn_{aus} can be observed in the gradual increase of the Mn content from which there is a direct drop to Mn_{fer} in Fig. 11.

Based on these results, ferrite seems to be absent only at the very start of the oxidation process, because not enough Mn was depleted to allow ferrite formation. When Mn content at the interface reached the Mn_{aus} threshold, ferrite formed. Between Mn_{aus} and Mn_{fer}, both phases are stable with this specific Mn partition; therefore, Mn content dropped directly between these two values at the ferrite/austenite interface. The Mn_{aus} and Mn_{fer} values were not the same during the entire process, changing due to Cr depletion. But, as shown in Fig. 9, these changes were not large. The ferrite layer thickened as Mn was consumed by oxidation, as Fig. 10b shows. When the samples were cooled, Mn diffused from austenite to ferrite and Mn_{aus} increased. The difference between the Mn concentration profile at the oxidation temperature and after cooling was small (Fig. 11), suggesting that characterizations at room temperature are sufficient, especially considering ferritic layer thickness and average Mn composition.

5. Conclusions

Understanding and controlling the mechanisms by which Mn-depleted ferritic layers form in FeMnSiCrNi alloys can allow the development of new oxidation-resistant alloys or treatments that can enhance their oxidation resistance. Here, an empirical relationship between ferritic layer thickness and mass variation was shown. The relationship was valid not only for the alloys studied here but for various other FeMnSiCrNi alloys. This can be used to estimate ferritic layer thickness in FeMnSiCrNi alloys. Results showed that contrary to what was believed to occur with some previously studied alloys, ferrite forms at the oxidation temperature for the alloys studied here. Thus, ferrite formation should be considered when evaluating the high-temperature oxidation behavior of similar alloys. In this study, although a ferritic layer was always present during oxidation, the mass gain of the alloy with more ferritizing elements (Cr and Si) was higher in some temperatures, despite the protective capabilities of these elements during high-temperature oxidation. Thus, the readiness with which ferrite forms can also increase the oxidation rate in some temperatures through mechanisms that will be investigated in-depth in further studies. Finally, the Mn concentration profile observed at room temperature was only slightly different than the one observed at the oxidation temperature. Therefore, characterizations of this layer at room temperature are sufficient to determine its general features (thickness, Mn content) during oxidation for alloys in which ferrite is stable during oxidation.

Declaration of competing interest

The authors declare the following financial interests/personal relationships which may be considered as potential competing interests: Joao Gabriel da Cruz Passos reports financial support was provided by Coordination of Higher Education Personnel Improvement.

Acknowledgments

The authors would like to thank CAPES (Coordination of Superior Level Staff Improvement) for providing a master's scholarship.

REFERENCES

[1] Alaneme KK, Okotete EA. Reconciling viability and cost-effective shape memory alloy options – a review of copper and iron based shape memory metallic systems. Engineering Sci Technol International J 2016;19(3):1582–92. https://doi.org/10.1016/j.jestch.2016.05.010.

[2] Otsuka H, Yamada H, Maruyama T, Tanahashi H, Matsuda S, Murakami M. Effects of alloying additions on Fe-Mn-Si shape memory alloys. ISIJ Int 1990;30(8):674–9. https://doi.org/10.2355/isijinternational.30.674.

[3] Ma R, Peng H, Wen Y, Zhang L, Zhao K. Oxidation behavior of an austenitic stainless FeMnSiCrNi shape memory alloy. Corrosion Sci 2013;66:269–77.

[4] Sousa Malafaia AM de, Da Silva R, Della Rovere CA, Baldan R, Suárez-Fernández L, Cabrera-Marrero J-M, et al. High temperature cyclic oxidation behavior of a low manganese Fe12Mn9Cr5Si4Ni-NbC shape memory stainless steels. J Alloys Compd 2021;857:158198. https://doi.org/10.1016/j.jallcom.2020.158198.

[5] Souza VF de, Araújo AJ, Santos Josué, Nascimento Lucas do, Della Rovere CA, Malafaia Artur, et al. Kinetics oxidation and characterization of cyclically oxidized layers at high temperatures for FeMnSiCrNiCe and FeSiCrNi alloys. Mater Res 2017;20(suppl 2):365–73. https://doi.org/10.1590/1980-5373-mr-2017-0098.

[6] Silva R, Vacchi GS, Santos IGR, Sousa Malafaia AM de, Kugelmeier CL, Mendes Filho AA, et al. Insights into high-temperature oxidation of Fe-Mn-Si-Cr-Ni shape memory stainless steels and its relationship to alloy chemical composition. Corrosion Sci 2020:163.

[7] Douglass DL, Rizzo-Assuncao F. The oxidation of Fe-19.6Cr-15.1Mn stainless steel. Oxid Met 1988;29:271–87.

[8] Marasco AL, Young DJ. The oxidation of Iron-Chromium-Manganese alloys at 900°C. Oxid Met 1991;36:157–74.

[9] Da Cruz Passos JG, Rabelo LFP, Freitas BX de, Da Silva R, Della Rovere CA, Sousa Malafaia AM de. Effects of silicon and manganese content on the oxidation behavior of FeMnSiCrNi alloys and the correlation between Mn-depleted zone, surface roughness and oxidation resistance. Corrosion Sci 2021:109724. https://doi.org/10.1016/j.corsci.2021.109724.

[10] Silva R, Arana C, Sousa Malafaia AM de, Mendes Filho AA, Pascal C, Otubo J, et al. Microstructure and surface oxidation behavior of an austenitic Fe-Mn-Si-Cr-Ni-Co shape memory stainless steel at 800 °C in air. Corrosion Sci 2019;158:108103. https://doi.org/10.1016/j.corsci.2019.108103.

[11] Sousa Malafaia AM de, Latu-Romain L, Wouters Y. FeMnSiCrNi oxidation at 800 °C: mechanism and characterization of improved oxidation resistance generated by vacuum annealing treatment. Oxid Met 2021;96(1–2):17–29. https://doi.org/10.1007/s11085-021-10038-7.

[12] Rabelo L, Silva R, Della Rovere CA, Sousa Malafaia AM de. Metal/oxide interface roughness evolution mechanism of an FeMnSiCrNiCe shape memory stainless steel under high temperature oxidation. Corrosion Sci 2020;163:108228. https://doi.org/10.1016/j.corsci.2019.108228.

[13] Sousa Malafaia AM de, Nascimento VR, Souza LM, Silveira ME, Oliveira MF. Anomalous cyclic oxidation behaviour of an Fe-Mn-Si-Cr-Ni alloy - a finite element analysis. Corrosion Sci 2019;147:223–30.

[14] Jiao Y, Zhang H, Wen Y. Influence of temperature on the oxidation behaviour of an austenitic stainless FeMnSiCrNi shape memory alloy. Oxid Met 2019;92(1–2):109–21. https://doi.org/10.1007/s11085-019-09916-y.

[15] Coccia Lecis G, Lenardi C, Sabatini A. The effect of Mn-depleted surface layer on the corrosion resistance of shape memory Fe-Mn-Si-Cr alloys. Metall Mater Trans 1997;28A:1219–22.

[16] Sousa Malafaia AM de, Latu-Romain L, Wouters Y. High temperature oxidation resistance improvement in an FeMnSiCrNi alloy by Mn-depletion under vacuum annealing. Mater Lett 2019;241:164–7.

[17] Sousa Malafaia AM de, Latu-Romain L, Wouters Y. Initial stages of FeMnSiCrNi shape memory stainless steels oxidation mechanism at 800 °C. Corrosion Sci 2021;181:109255. https://doi.org/10.1016/j.corsci.2021.109255.

[18] Jung I-H. Critical evaluation and thermodynamic modeling of the Mn–Cr–O system for the oxidation of SOFC interconnect. Solid State Ionics 2006;177:765–77.

[19] Smith AF, Hales R. The diffusion of chromium in a duplex alloy steel. Met Sci 1976;10(12):418–23. https://doi.org/10.1179/030634576790431859.